Computational Materials Science 218 (2023) 111950

Contents lists available at ScienceDirect

Computational Materials Science

journal homepage: www.elsevier.com/locate/commatsci

Full Length Article

A comprehensive study of defects in gallium oxide by density functional theory

Mohi Uddin Jewel, Samiul Hasan, Iftikhar Ahmad *

Department of Electrical Engineering, University of South Carolina, Columbia, SC 29208, USA

ARTICLE INFO

Keywords:
Density Functional Theory
Defects
Gallium Oxide
Formation Energy
Raman Spectroscopy

ABSTRACT

Ultrawide bandgap gallium oxide (Ga_2O_3) is a promising material for power semiconductor devices and deep ultraviolet (UV) solar-blind photodetectors. Understanding the properties of point defects in Ga_2O_3 is necessary to realize better-performing devices. A comprehensive study based on density functional theory (DFT), using the generalized gradient approximation (GGA): Perdew-Burke-Ernzerhof (PBE) exchange–correlation functional, of point defects in corundum (α), monoclinic (β), and orthorhombic (ε) phases of Ga_2O_3 is presented. The point defects include vacancies, interstitials, antisites, and extrinsic impurities in various phases of Ga_2O_3. Defect formation energies, charge transition energy levels, and defect concentrations variation with temperature are listed and presented under both gallium-rich (Ga-rich) and oxygen-rich (O-rich) growth conditions. The formation energy diagrams predict that the Ga_2O_3 phases favor the formation of Ga and O vacancies and the incorporation of extrinsic impurities. The calculations also show that the charge transition levels are deep inside the bandgap regardless of the Ga_2O_3 phase and growth environment. The impacts of temperature on the intrinsic point defects are analyzed by probing the vibrational modes of β-Ga_2O_3 thin films grown in a metal–organic chemical vapor deposition (MOCVD) system at 700 °C temperature and annealed at 1100 °C in an O-rich environment.

1. Introduction

Recently there has been increasing research interest in gallium oxide (Ga_2O_3) based materials and devices [1]. The emergence of wide and ultrawide bandgap (UWBG) semiconductors such as III-nitrides (GaN, AlGaN), silicon carbide (SiC), diamond (C), including gallium oxide (Ga_2O_3) has spurred the development of the new class of light emitting diodes (LEDs) [2,3], power semiconductor devices [4], and deep-ultraviolet (UV) solar-blind photodetectors [5]. Despite the low thermal conductivity, Ga_2O_3 has a large Baliga-Figure-of-Merit [6,7]. The Ga_2O_3 is an UWBG semiconductor with five polymorphs [1], namely the corundum (α), monoclinic (β), orthorhombic (ε), defective spinel (γ), and cubic (δ) phases having the bandgap of α, β, ε-Ga_2O_3 exceeding 3.25 eV [8–11]. These phases of Ga_2O_3 were grown using various growth methods and have many useful applications [8,12–20]. All the phases of Ga_2O_3, regardless of the growth mechanism, have defects that can be studied theoretically and experimentally.

Each phase of Ga_2O_3 has a specific relaxation energy, which determines its stable structure. The α-, ε-, and γ- phases are metastable structures and can transform into more stable β-phase [21]. The phase transformation follows α → β or ε → β or γ → α → β or γ → β transitions under proper ambient and temperature [21]. Moreover, these phases can coexist within a thin film [22]. The thin films and devices of metastable phases can be stabilized by adjusting the growth parameters and methods [8,19,20,23]. The thin films and devices based on different phases of Ga_2O_3 get adversely affected by the point defects. The density functional theory (DFT) or first principles calculation is a powerful simulation framework to determine the electronic as well as interface properties and defects of semiconductors [24]. The DFT with semilocal exchange–correlation functional like the local density approximation (LDA) and generalized gradient approximation (GGA) can provide valuable quantitative and qualitative information about the defect formation energies and charge transition levels for oxide materials [25]. The properties like band structures [26], carrier transport [27,28], doping [29,30], two-dimensional electron gas (2DEG) formation [31], and defects [29] in Ga_2O_3 were reported using the DFT. Although the

Abbreviations: DFT, Density Functional Theory; UWBG, Ultrawide Bandgap; GGA, Generalized Gradient Approximation; PBE, Perdew-Burke-Ernzerhof; MOCVD, Metal Organic Chemical Vapor Deposition; LED, Light Emitting Diode; LDA, Local Density Approximation; FNV, Freysoldt – Neugebauer - Van de Walle.

* Corresponding author.
E-mail address: ahmad@cec.sc.edu (I. Ahmad).

https://doi.org/10.1016/j.commatsci.2022.111950
Received 28 August 2022; Received in revised form 17 November 2022; Accepted 27 November 2022
Available online 2 December 2022

DFT calculations with LDA or GGA approaches have intrinsic shortcomings such as bandgap underestimation, electron self-interaction errors, and their inability to properly delocalize the electrons, but still a very useful tool to understand the properties of semiconductor materials [24]. The hybrid functional formed by adding a Hartree-Fock exchange term in the semilocal functional corrects the self-interaction errors and produces a bandgap close to the experimental value [32]. These advantages come with a significant computational expense. The Hubbard correction on which DFT + U (U is Coulomb interaction potential) scheme is built, can also resolve some of these shortcomings [33]. While DFT and DFT + U have comparable computational cost once U-parameters are determined, the U-parameters need separate optimization for different phases of Ga_2O_3, supercell and defectives structures, and their charge states which increase computational complexity and cost. The individual theoretical studies on defect properties of Ga_2O_3 with hybrid functionals covered narrow aspects of defects, usually vacancies, interstitials [34], and p- or *n*-type doping in a single Ga_2O_3 structure [29,30]. Takuma et al. reported the formation energies and charge transition levels for Ga and O vacancies and interstitials (V_{Ga}, V_O, Ga_i, O_i) in α-Ga_2O_3 [35]. Zacherle et al. studied the V_{Ga}, V_O, Ga_i, O_i defect properties in β-Ga_2O_3 [34]. The scope of p- and *n*-type dopants for α- and β-Ga_2O_3 was also reported with hybrid functional DFT [29,30]. The results can be different with diverse DFT parameterization and selection of DFT software packages. A comprehensive study of the defect properties in various Ga_2O_3 phases, including antisite and extrinsic defects, is still warranted to alleviate the patchwork in reporting the point defects and their formation energies, charge transition levels, and related experimental perspectives.

We performed a comprehensive study of point defects, including vacancies, interstitials, antisites, and extrinsic impurities, in the α-, β-, ε-Ga_2O_3 using the DFT implemented in QUANTUM ESPRESSO software. Such large-scale studies with hybrid functional demand high computational costs. Considering the trade-off between computational cost and accuracy, we used generalized gradient approximation (GGA): Perdew-Burke-Ernzerhof (PBE) exchange–correlation functional for the DFT calculations. The lower-cost GGA: PBE with band-edge correction schemes are expected to produce qualitatively and quantitatively correct predictions, as did for GaN and hafnia (HfO_2) [24,25]. To qualitatively describe and correlate the impact of temperature on the point defects, we probed the vibrational modes of β-Ga_2O_3 thin films grown in a metal–organic chemical vapor deposition (MOCVD) system at 700 °C and annealed at 1100 °C in an O-rich environment.

2. Ga_2O_3 crystal phases and band structures

The corundum α-Ga_2O_3 belongs to the trigonal *R*-3*c* space group (a = 5.05952 Å, c = 13.62480 Å, α = β = γ = 90°). Ga_1 is bonded to six equivalent O_1 atoms to form a mixture of distorted edge, face, and corner-sharing GaO_6 octahedra, as shown in Fig. 1a. Each conventional unit cell of α-Ga_2O_3 has 30 atoms. The Brillouin zone has a high symmetry path along Γ—T—H_2|H_0—L—Γ—S_0|S_2—F—Γ points. The α-Ga_2O_3 has an indirect bandgap of 2.25 eV, as shown in Fig. 2a. The bandgap shows a lower value as compared to experimental values as the band structure is calculated using GGA functional only. The β-Ga_2O_3 has the monoclinic structure with *C*2/*m* space group (a = 12.45245 Å, b = 3.08297 Å, c = 5.87615 Å, α = γ = 90°, β = 103.6836°). The β-Ga_2O_3 has two distinct Ga- sites, namely Ga_1 and Ga_2, and three distinct O- sites, namely O_1, O_2, and O_3. Ga_1 atoms are bonded to two equivalent O_1, one O_2, and one O_3 to form a tetrahedral arrangement, as shown in Fig. 1(b). Ga_2 atoms are bonded to one O_1, three equivalent O_2, and two

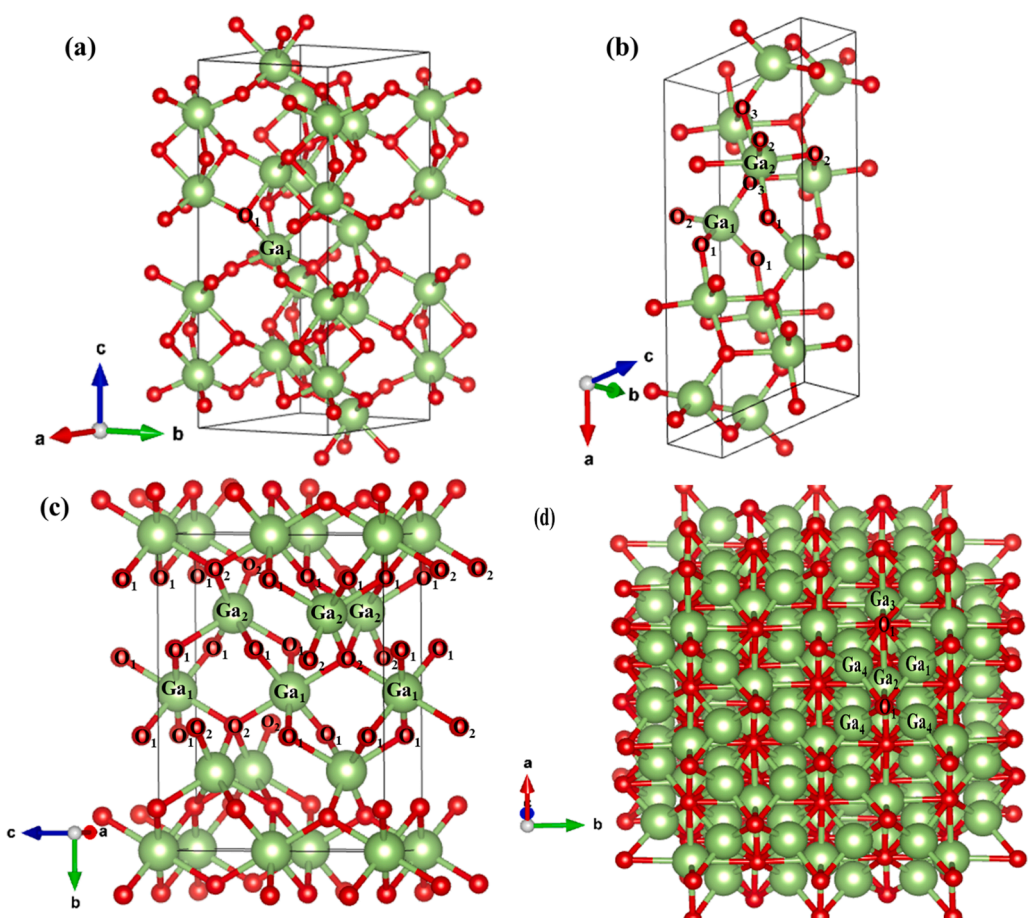

Fig. 1. Conventional unit cell structure of (a) α-Ga_2O_3, (b) β-Ga_2O_3, (c) ε-Ga_2O_3, and (d) γ-Ga_2O_3.

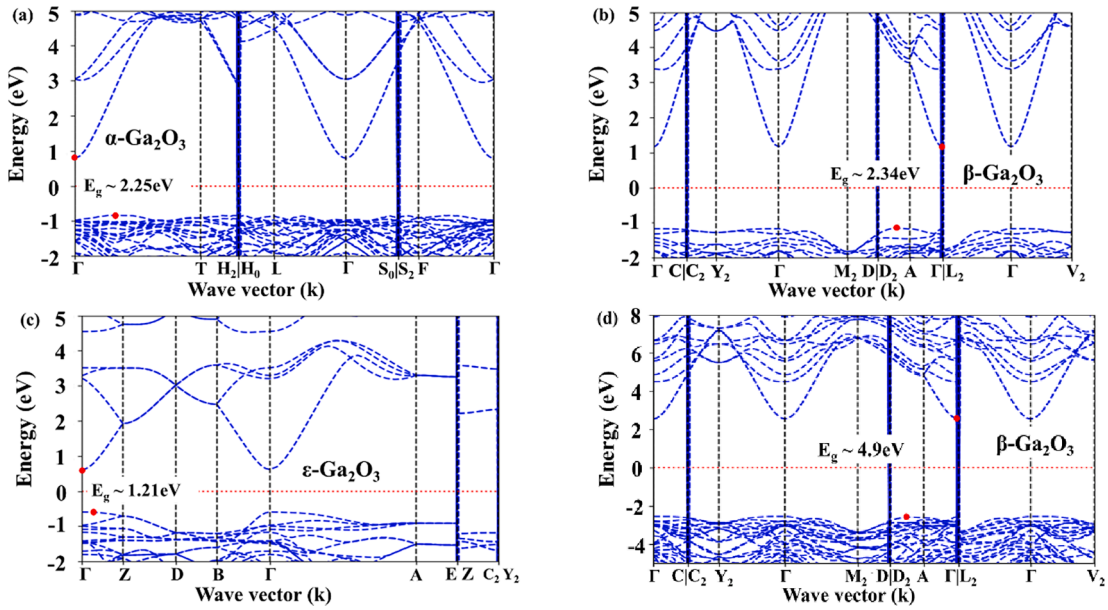

Fig. 2. Calculated band diagram using GGA functional for (a) α-Ga_2O_3, (b) β-Ga_2O_3, and (c) ε-Ga_2O_3 structures, and (d) band structure of β-Ga_2O_3 using Hubbard correction or DFT + U method.

equivalent O_3 atoms to form an octahedral arrangement. Each conventional unit cell of β-Ga_2O_3 has 20 atoms. The Brillouin zone has a high symmetry path along Γ—C|C_2—Y_2—Γ—M_2—D|D_2—A—Γ|L_2—Γ—V_2 points. The β-Ga_2O_3 has an indirect bandgap of 2.34 eV as shown in Fig. 2b. The orthorhombic ε-Ga_2O_3 (also referred to as κ-phase) crystallizes in the orthorhombic CmCm space group (a = 2.82039 Å, b = 9.39439 Å, c = 7.28403 Å, α = β = γ = 90°). The structure has two inequivalent Ga- sites, namely Ga_1 and Ga_2, and two inequivalent O-sites labeled as O_1 and O_2, as shown in Fig. 1c. Ga_1 bonds with four neighboring O_1 and two O_2 atoms. Ga_2 atoms bond with four O_1 and two O_2 atoms to form a mixture of edge and corner-sharing GaO_6 octahedra. Each conventional unit cell of ε-Ga_2O_3 has 20 atoms. The Brillouin zone has a high symmetry path along Γ—Z—D— B—Γ—A—E—Z—C_2—Y_2 points. The ε-Ga_2O_3 has a bandgap of 1.21 eV, as shown in Fig. 2c. The defective spinel γ-Ga_2O_3 takes the cubic shape with Fd3$\bar{m}$ space group as shown in Fig. 1d [20]. Each conventional unit cell of γ-Ga_2O_3 has 120 atoms. There are four inequivalent Ga sites. The γ-Ga_2O_3 does not have a bandgap. Overlapping bands along high symmetry points on the DFT band structure confirmed the absence of bandgap in γ-Ga_2O_3. Thereby, we restricted all DFT calculations and discussions related to the α-, β-, and ε-phases only. The experimental bandgap can be generated with hybrid functional or Hubbard correction, aka DFT + U scheme, where U is the Coulomb interaction potential. Using DFT + U and setting the U_d value for the 3d valence electrons of Ga equal to 7 eV, and the U_p value for 2p valence electrons of O equal to 7.9 eV, a bandgap of 4.9 eV is calculated for β-Ga_2O_3 and shown in Fig. 2d, giving us the confidence in our calculations. Defect calculations with hybrid functional or DFT + U are computationally costly (high cost comes from U-parameters optimization for DFT + U) for a comprehensive study; hence we employ GGA functional for all our calculations.

3. Computational approach

The detailed scheme of our calculations is shown in Figure S1 (Supplementary Information) as a flowchart. The calculations have two major steps: i) perform DFT simulation to compute the formation energies for all defects with various charge states, and ii) Use self-consistent Fermi energy (E_F) and charge neutrality equation to calculate the Fermi level (E_F), defects concentration, and electron and hole concentrations (n_o and p_o). All DFT calculations are performed using generalized gradient approximation (GGA): Perdew-Burke-Ernzerhof (PBE) exchange–correlation functional with plane-wave basis sets as implemented in open-source QUANTUM ESPRESSO package [36,37]. The standard solid-state pseudopotentials (SSSP) for Ga, O, Si, and Mg are used for calculations [38]. The plane-wave cutoff energies are set at 45 Ry (~600 eV). Spin polarization is not considered. A 120 atoms supercell is sufficient to produce a well-converged defect formation energy in Ga_2O_3 materials [34,35]. The total energies of bulk and defective structures are obtained from the variable-cell relaxation of 120-atom supercells of α, β, ε-Ga_2O_3 using the 2 × 2 × 2 Monkhorst-Pack k-point mesh.

Considering an extended Ga_2O_3 thermodynamically equilibrium material system in which defects can form. All the point defects can be present in Ga_2O_3. One or two types of point defects with the lowest defect formation energy typically contribute largely to the total point defect concentration depending on growth conditions. The Ga_2O_3 material contains a set of point defects {X}. The {X} can be Ga or O vacancies (V_{Ga} or V_O), Ga or O interstitials (Ga_i or O_i), Ga or O antisites, like gallium at oxygen site (Ga_O) or oxygen at gallium site (O_{Ga}), and silicon (Si) or magnesium (Mg) dopants (Si_{Ga} or Mg_{Ga}). There are different numbers of Ga and O sites in β-Ga_2O_3 and ε-Ga_2O_3 for which vacancies were marked as V_{Ga1}, V_{O1}, and such. These defects can acquire + / −1 or + / −2 or + / −q electronic charge states if the defective system leaves/accepts that many electrons. The formation of defects is associated with adding or removing an atom to or from a reservoir. The formation energy of a defect is the change in Gibbs free energy, $\Delta G(X^q) = \Delta H(X^q) - T\Delta S(X^q)$ where T is temperature, ΔH is enthalpy, and ΔS is entropy [39]. We assume these defects to form in the dilute limit; hence they are non-interacting. The entropic contribution (TΔS) in ΔG is at least one order lower than the enthalpic contribution (ΔH) [40]. Ignoring the entropic term, the formation energy $\Delta E_f(X, q, E_F)$ of defect {X} with charge state q is the Gibbs free energy and expressed as [25,34,35,39]

$$\Delta E_f(X,q,E_F) = E_{TOTAL}(Defective) - E_{TOTAL}(Bulk) + \sum n_i\mu_i + q(E_{VBM} + E_F \pm \mu_e) + E_{corr} \quad (1)$$

where $E_{TOTAL}(Defective)$ is the total energy of the defective supercell obtained from the DFT, $E_{TOTAL}(Bulk)$ is the total energy of the perfect

crystal supercell obtained from the DFT, i is the atomic species, n_i is the number of atoms added (negative) or removed (positive) from the host supercell, μ_i is the chemical potential, E_{VBM} is the energy of the valence band maximum (VBM), E_F is the Fermi level referenced to E_{VBM}, μ_e is the electron chemical potential accounting the shift in Fermi level referenced to $E_{VBM,}$ and E_{corr} relates to an image charge correction for the finite size of the charged supercells.

The chemical potential μ_i is the potential energy, $E_{total}(i)$ related to an atom or a molecular structure. The energy of a silicon atom, μ_{Si} is taken as 1/64th of bulk energy in a 64-atoms cubic Si supercell with a 4 × 4 × 4 k-point grid. The chemical potential of magnesium μ_{Mg} is calculated as 1/54th of bulk energy in a 54-atoms cubic Mg supercell with a 4 × 4 × 4 k-point sampling. The chemical potential of gallium μ_{Ga} is taken as 1/36th of bulk energy in a 36 atoms monoclinic Ga supercell with a 6 × 6 × 6 k-point mesh, i.e., $\mu_{Ga} = E_{total}(Ga) = \frac{E_{total}(36atoms)}{36}$. The μ_O is the oxygen atom chemical potential which is calculated as half of the energy of the oxygen molecule (O_2) in its triplet state, i.e., $\mu_O = E_{total}(O) = \frac{E_{total}(O_2)}{2}$. We consider two extreme crystal growth conditions: gallium-rich (Ga-rich) and oxygen-rich (O-rich). The limits of chemical potentials are calculated from the chemical reaction of defect-free bulk Ga_2O_3, which is 2 Ga + $\frac{3}{2}O_2$= Ga_2O_3. The chemical potentials for Ga-rich conditions are $\mu_{Ga}^{Ga-rich} = \mu^{Ga} = E_{total}(Ga)$ and $\mu_o^{Ga-rich} = \frac{1}{3}[E_{total}(Ga_2O_3) - 2E_{total}(Ga)]$. The chemical potentials for O-rich conditions are $\mu_O^{O-rich} = \mu^O = E_{total}(O) = \frac{1}{2}E_{total}(O_2)$ and $\mu_{Ga}^{O-rich} = \frac{1}{2}[E_{total}(Ga_2O_3) - 3E_{total}(O)]$ where $E_{total}(i)$ is the energy of an element or compound obtained from DFT simulation. All calculations satisfied these necessary conditions: $\mu_{Ga}^{O-rich} \le \mu_{Ga} \le \mu_{Ga}^{Ga-rich}$ and $\mu_O^{Ga-rich} \le \mu_O \le \mu_O^{O-rich}$. Finite-size correction term E_{corr} is calculated with Freysoldt – Neugebauer - Van de Walle (FNV) correction scheme using the 'sxdefectalign' module [41,42]. The dielectric constants of the host material needed to execute the FNV scheme are collected from the literature and used for α [43], β [44], ε [31]- Ga_2O_3 supercells.

A thermodynamic charge transition level $\epsilon(q_1/q_2)$ is the Fermi-level position for which charge states q_1 and q_2 have equal defect formation energy. The $\epsilon(q_1/q_2)$ is given by [29]

$$\in\left(\frac{q_1}{q_2}\right) = \frac{\Delta E_f^{q_1}|_{E_F=0} - \Delta E_f^{q_2}|_{E_F=0}}{q_1 - q_2} \tag{2}$$

where $E_f^q|_{E_F=0}$ is the formation energy of the defect in a charge state q evaluated at $E_F = 0$. Using the calculated $\Delta E_f\ (X, q, E_F)$ for all the defects with various charge states, it is possible to determine the self-consistent Fermi level, individual defect concentration, electron, and hole carrier concentrations. The flowchart of the self-consistent calculation is shown in Figure S1 (Supplementary Information), and detailed algorithms are described by J. Buckeridge [39]. If n_o and p_o are the electron and hole concentrations, E is energy, E_g is material bandgap, $\rho(E)$ is the density of states per unit volume, k is Boltzmann constant, T is temperature, the Fermi-Dirac distribution function is $f_e(E) = \frac{1}{1+e^{(E-E_F)/kT}}$. The electrons and hole concentrations are expressed as [39],

$$n_0 = \int_{E_g}^{\infty} f_e(E)\rho(E)dE \tag{3}$$

$$p_0 = \int_{-\infty}^{0} [1 - f_e(E)]\rho(E)dE \tag{4}$$

Assuming that defect X and its charge states have a concentration of C_{X^q}, N_X is the number of possible defect sites, and g_{X^q} is the degeneracy factor considering both the spin and structural degeneracy in III-oxide materials [45], then the equilibrium defect concentration is given by [25]

$$C_{X^q} = N_X g_{X^q} e^{-\frac{\Delta E_f(X,q,E_F)}{kT}} \tag{5}$$

The charge neutrality condition implies the concentration of negative charges is equal to the concentration of positive charges. This condition remains valid for any semiconductor material in equilibrium. Considering the effect of defects and their charge states, the charge balance equation can be written as [39],

$$n_0(E_F) - \sum_X \sum_q qC_{X^q}(E_F) = p_0(E_F) \tag{6}$$

The n_o, p_o, and C_{X^q} are dependent on Fermi level E_F. The equations (3), (4), (5), and (6) can be solved self-consistently, and a self-regulated Fermi level E_F can be determined from the iterations. Then n_o, p_o, and C_{X^q} can be calculated as a function of temperature T.

4. Results and discussion

The point defects differ in type, lattice site, and charge state. There are two possible atomic vacancies in Ga_2O_3. The gallium Ga and oxygen O vacancies are introduced for each non-equivalent lattice site as seen in symmetric structures (Fig. 1a-c) and named as $V_{G_1}, V_{Ga_2}, V_{Ga_3}, V_{O_1}$ and V_{O_2} depending on the Ga_2O_3 phase. The low-energy positions for gallium interstitials Ga_i and oxygen interstitials O_i for the α-, β- Ga_2O_3 are available in the literature [34,35]. The most favorable interstitial sites for ε-Ga_2O_3 are identified from four possible interstitial positions. For Ga_O antisite (Ga-replace-O antisite), the O_1 lattice sites are used, and for O_{Ga} antisite (O-replace-Ga antisite) Ga_1 sites are used. For Si and Mg substitution, the Ga_1 lattice sites are used for all phases. The Si or Mg substitution in a Ga lattice site provides or lacks one electron to the crystal; hence Si is known as an *n*-type dopant and Mg as a *p*-type dopant. The defects are introduced to positions close to the center of the supercells. Table 1 charts the defect formation energy values obtained from DFT calculations for eight types of point defects in their charge-neutral state in two extreme crystal growth conditions (Ga-rich and O-rich). Our calculated formation energies for vacancies in β-Ga_2O_3 at charge neutral state are similar to values reported by GGA:PBE functional elsewhere [34]. The values from reference 36 are listed in brackets along with our calculations in a Ga-rich environment for comparison:- V_{O_1} : 1.168 eV (1.15 eV), V_{O_2}: 1.347 eV (1.34 eV), V_{O_3}: 0.78 eV (0.63 eV), V_{Ga_1}: 9.45 eV (9.03 eV), V_{Ga_2}: 9.693 eV (9.31 eV) [34]. In our calculations, the charge states from −3 to + 2 are considered for most of these defects.

Formation energy diagrams of point defects as a function of Fermi level under Ga- and O-rich conditions for corundum, monoclinic, and orthorhombic phases are shown in Fig. 3. The $E_F = 0$ corresponds to the E_{VBM}. The slope of the diagram represents the charge state of the defect. The bandgap of different phases of Ga_2O_3 obtained from GGA: PBE is shown as dashed lines in the formation energy diagrams. Regardless of the phase and growth conditions, the Ga_2O_3 favors the substitution with Si and Mg dopants and their various charge states. A formation energy diagram represents thermodynamically favorable charge states of a defect as a function of Fermi level E_F. For example, V_{O_1} defect in β-Ga_2O_3 follows the '+2'→ '0'→ '-1' →'-2' charge state sequence as a function of E_F. The '+1' charge state is difficult to form for V_{O_1} defect since it has other thermodynamically favorable charge states. In a Ga-rich environment, the V_{O_1} in α-Ga_2O_3 is the dominant defect since its charge states have relatively low formation energy than other defects. The Ga_i and Ga_O defects also have low defect formation energies at low E_F in the corundum structure. The V_{Ga_1} has comparatively lower formation energy at higher E_F. The V_{O_1}, V_{O_2}, and V_{O_3} are the dominant defects in β-Ga_2O_3. The Ga_i and Ga_O defects also have low defect formation energies at low E_F in β-Ga_2O_3. The V_{O_1}, V_{O_2}, and V_{Ga_1} have lower formation energies in ε-Ga_2O_3. In all phases, the O_i and O_{Ga} have high defect formation energies, making them unlikely to occur in a Ga-rich environment. Some intrinsic defects, for example, oxygen vacancies in all phases, have negative formation energies at low E_F. This implies that these defects will form spontaneously. In an O-rich environment, the V_{O_1}, V_{Ga_1} are dominant defects with moderate contributions from O_{Ga} in α-Ga_2O_3. The Ga_O defect charge states have lower formation energy in

Table 1
Defect formation energy in eV at charge neutral state for various point defects in α-, β-, and ε-Ga_2O_3.

Phase		V_{O_1}	V_{O_2}	V_{O_3}	V_{Ga_1}	V_{Ga_2}	O_i	Ga_i	Ga_O	O_{Ga}	Mg_{Ga}	Si_{Ga}
α-Ga_2O_3	Ga-rich	1.511	——	——	9.114	——	8.220	6.012	5.836	12.138	0.087	−0.82
	O-rich	4.943	——	——	3.967	——	4.788	11.159	14.41	3.559	−5.06	−5.96
β-Ga_2O_3	Ga-rich	1.168	0.78	1.347	9.450	9.693	1.946	5.049	4.045	11.556	0.331	−1.605
	O-rich	4.637	4.25	4.816	4.246	4.489	5.415	10.253	12.71	2.884	−4.87	−6.81
ε-Ga_2O_3	Ga-rich	1.148	1.374	——	6.126	6.128	5.635	6.128	5.333	12.314	−0.88	−2.07
	O-rich	4.161	4.387	——	1.563	1.608	2.621	1.608	12.87	4.7816	−5.40	−6.584

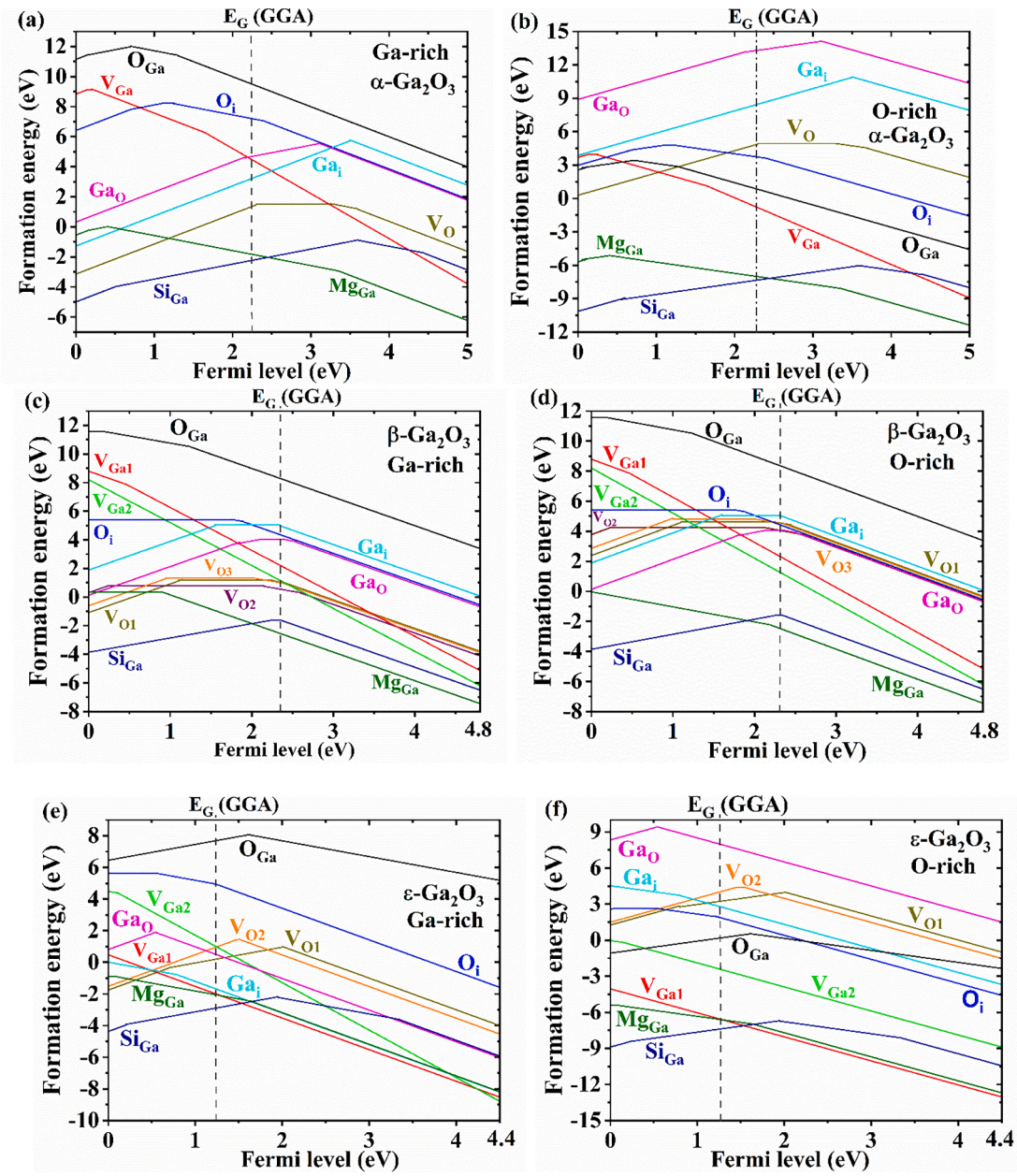

Fig. 3. Formation energies of defects in corundum, monoclinic, and orthorhombic phases of Ga_2O_3 in Ga-rich and O-rich conditions. Bandgaps calculated from DFT GGA: PBE is represented by dash lines.

β-Ga_2O_3. The V_{Ga_1} and V_{Ga_2} are dominant defects in ε-Ga_2O_3 with negative formation energies, prompting their spontaneous formation and possibly making the ε-Ga_2O_3 phase metastable [19].

The transition between the q_1 and q_2 charge state can be introduced using light, heat, or a combination of both. It is possible to realize charge transition levels from the formation energy diagram. Table 2 and Fig. 4 show the derived charge transition levels for all point defects in three Ga_2O_3 phases. It is noteworthy that the transition levels $\epsilon(q_1/q_2)$ are independent of growth conditions (Ga-/O-rich). We can determine these levels experimentally through techniques like deep-level transient

Table 2
Charge transition energy levels in eV for various phases of Ga_2O_3 when charge state changes from q_1 to q_2.

Phase	q_1	q_2	V_{O_1}	V_{O_2}	V_{O_3}	V_{Ga_1}	V_{Ga_2}	O_i	Ga_i	Ga_O	O_{Ga}	Mg_{Ga}	Si_{Ga}
α-Ga_2O_3	2	1	—	—	—	—	—	0.70	—	2.177	0.153	0.155	0.506
	2	0	2.326	—	—	0.15	—	—	—	—	—	—	—
	2	−2	—	—	—	—	—	—	3.531	—	—	—	—
	1	−2	—	—	—	—	—	—	—	3.114	—	—	—
	1	0	—	—	—	—	—	1.111	—	—	—	—	—
	1	−1	—	—	—	—	—	—	—	—	0.731	0.403	3.603
	0	−1	3.282	—	—	—	—	1.223	—	—	—	—	—
	0	−2	—	—	—	0.227	—	—	—	—	—	—	—
	−1	−2	3.631	—	—	—	—	2.415	—	—	1.311	3.35	4.453
	−2	−3	—	—	—	1.652	—	—	—	—	—	—	—
β-Ga_2O_3	2	1	—	—	—	—	—	—	—	1.803	—	—	—
	2	0	1.123	0.264	0.976	—	—	—	1.575	—	—	—	—
	1	0	—	—	—	—	—	—	—	2.136	0.011	—	2.250
	0	−1	2.236	2.258	2.00	—	—	1.751	2.321	2.372	0.203	—	—
	0	−2	—	—	—	—	—	—	—	—	—	0.905	2.348
	−1	−2	2.407	2.615	2.398	—	—	1.912	2.366	2.507	1.254	—	—
	−2	−3	—	—	—	0.453	—	—	—	—	—	—	—
ε-Ga_2O_3	2	1	0.701	—	—	—	—	—	—	—	—	—	—
	2	0	—	1.453	—	—	—	—	—	—	—	—	—
	2	−2	—	—	—	—	—	—	—	0.562	—	—	—
	1	−2	2.022	—	—	—	—	—	—	—	—	—	—
	1	0	—	—	—	—	—	0.05	—	—	—	—	—
	1	−1	—	—	—	—	—	—	—	—	1.615	—	1.934
	0	−1	—	—	—	—	—	0.553	—	—	—	0.047	—
	0	−2	—	1.515	—	—	—	—	—	—	—	—	—
	−1	−2	—	—	—	—	—	1.267	0.794	—	—	1.662	3.361
	−1	−3	—	—	—	—	0.106	—	—	—	—	—	—

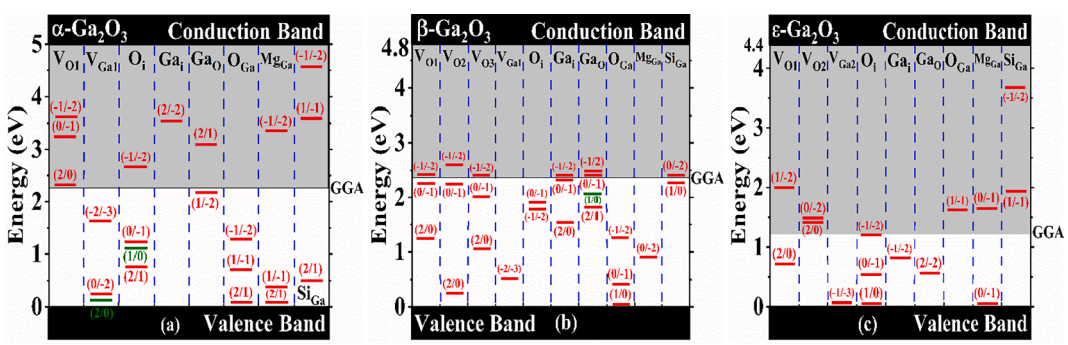

Fig. 4. The charge transition levels of point defects inside the bandgaps of (a) α-Ga_2O_3, (b) β-Ga_2O_3, and ε-Ga_2O_3 extended up to measured bandgap values (nearby transition levels are distinguished by red and green colors).

spectroscopy (DLTS). In α-Ga_2O_3, the transition levels are primarily below the midgap level for V_{Ga}, O_i, O_{Ga}, Mg_{Ga} defects, whereas the transition levels are above the midgap level for V_O, Ga_i, Ga_O, and Si_{Ga} defects. In β-Ga_2O_3, the charge transition levels are around or below the midgap for all the defects. In ε-Ga_2O_3, the charge transition levels remain mostly around or below the midgap. Some transition levels in V_{Ga}, O_i, O_{Ga}, and Mg_{Ga} are just above the E_{VBM}, but the energy difference with E_{VBM} is over 5kT (~130 meV), so, these transition levels are at deep levels.

In oxide materials, V_O, Ga_O, Ga_i are donor defects, and O_i, V_{Ga}, O_{Ga} are acceptor defects [46]. The defect concentration should be less than the available defect sites ($N_X \sim 10^{23}$ sites/cm^3). The Fermi level E_F, electron, and hole concentrations, and defect concentrations are calculated using the algorithm shown in Figure S1 (Supplementary Information). Fig. 5 shows the intrinsic defects concentration as a function of temperature in Ga- and O-rich environments. In α-Ga_2O_3, the concentration of V_O can be as high as 10^{20} cm^{-3} since V_O is the dominant defect in a Ga-rich environment. This pulls E_F slightly up to show the effect of donor defect. In an O-rich environment, the concentration of O_{Ga} can reach up to 10^{13} cm^{-3}. Also, with the minor acceptor defect type contribution from the V_{Ga} and O_i, the overall E_F for α-Ga_2O_3 lies inside the valence band, pulling E_F further inside with temperature to accommodate the acceptor defects. In β-Ga_2O_3, the V_{O_1}, V_{O_2}, and V_{O_3} are the dominant defects and their concentrations can get up to ~ 10^{21} cm^{-3} in Ga-rich environments. In an O-rich environment, the net effect originates from both donor and acceptor defects keeping the E_F almost constant through the temperature range. In the ε-Ga_2O_3, the negative formation energies for the V_{O_1}, V_{O_3} defects in a Ga-rich environment, and for the V_{Ga_1}, O_{Ga} defects in an O-rich condition result in defect concentration larger than the number of available sites for defect formation. This creates a logical discrepancy showing deviance in the assumption of non-interacting defects formation at the dilute limit [39]. Assuming a spontaneous formation of these defects by large numbers since they have negative formation energies, it is possible to determine the contribution of the rest of the defects. The Ga_O defect concentration in the ε-Ga_2O_3 can reach 10^{17} cm^{-3} with temperature in a Ga-rich environment. The V_{Ga_2} defect can have a concentration up to 10^{17} cm^{-3} followed by the contribution from the V_{O_1}, V_{O_2}, O_i defects at a 2–3 order lower rate as a function of temperature in an O-rich environment. The Fermi levels stay deep inside the valence band through the temperature range.

In theory, the intrinsic defect concentration keeps increasing with temperature (shown up to 1400 K), and the Ga-/O-rich condition is considered extreme. In experiments, the presence of Ga and O are

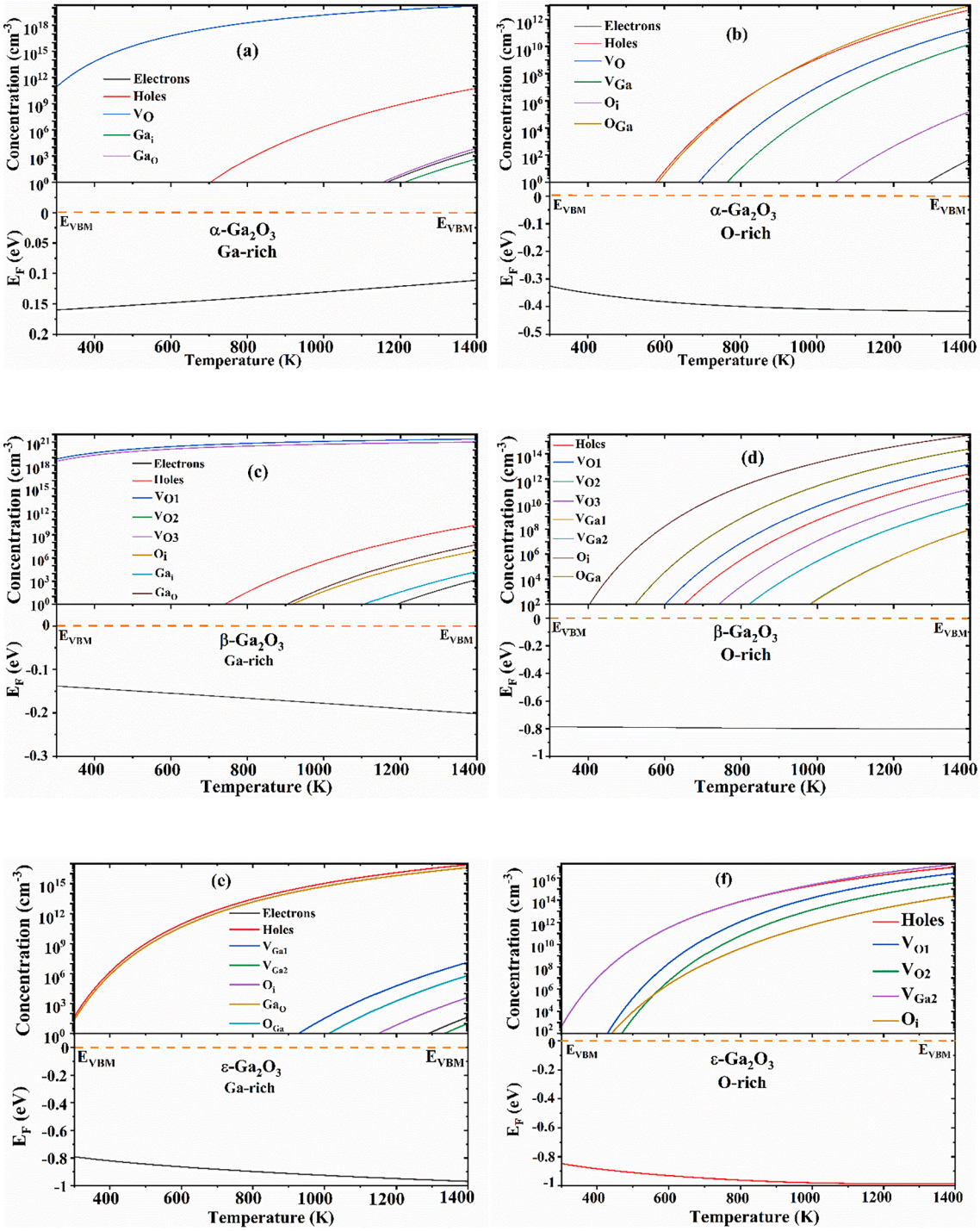

Fig. 5. Temperature dependent self-consistent Fermi level and intrinsic defect concentrations in Ga_2O_3.

optimized to obtain high-quality Ga_2O_3 thin films within a temperature window for each Ga_2O_3 phase. To correlate the defect properties from the DFT calculations, we performed spectroscopic measurements in an as-grown and a high-temperature annealed (in O-rich environment) β-Ga_2O_3. High-temperature thermal annealing of β-Ga_2O_3 in an oxygen (O_2) environment may increase the gallium vacancies (V_{Ga}) and oxygen interstitials (O_i), and reduce the oxygen vacancies (V_O) in the thin films [47,48]. Point defects affect the vibrational modes of materials which may appear as a new peak or a change in the width of the peak [49–51]. The β-Ga_2O_3 growth in the MOCVD system has a temperature window in the 650–850 °C range [52]. The β-Ga_2O_3 epilayers for this study were grown on a c-plane sapphire substrate in a cold-wall vertical MOCVD system at 700 °C using triethyl gallium (TEG) and oxygen gas (99.999 % purity) as precursors. The details of such growth can be found elsewhere [47]. The thickness of the sample is ~ 0.3 μm with a bandgap of ~ 4.8 eV as measured by ultraviolet–visible (UV–vis) spectroscopy. The β-Ga_2O_3 thin film has ($\bar{2}01$) X-ray diffraction (XRD) orientation. To emulate the defect behaviors in β-Ga_2O_3 in an O-rich environment, the grown epilayer was annealed at 1100 °C under 1000 sccm (standard cubic centimeter) oxygen (O_2) flow for 30 min in the same MOCVD reactor in which the sample was grown. The thickness, bandgap, and crystal orientation remained almost the same after annealing. The annealing process increases the V_{Ga} and O_i and reduces the V_O concentrations in the β-Ga_2O_3

thin film [47,48]. As shown in Fig. 6, Raman spectra are acquired using a Horiba Raman spectroscope with a 638 nm red laser excitation passing through a 50x objective lens in a backscattered mode with a spectral resolution of 0.5 cm^{-1}. The Raman spectra of the β-Ga_2O_3 samples exhibit the Raman phonon modes at 105.95 ($A_g^{(1)}$), 118.76 ($B_g^{(1)}$), 142.75 ($B_g^{(2)}$), 175.63 ($A_g^{(2)}$), 198.68 ($A_g^{(3)}$), 322.81 ($A_g^{(4)}$), 348.21 ($A_g^{(5)}$), 354.94 ($B_g^{(3)}$), 477.63 ($A_g^{(7)}$), 633.43 ($A_g^{(8)}$), 650.8 ($B_g^{(5)}$), 657.5 ($A_g^{(9)}$) cm^{-1}, and longitudinal phonon-plasmon coupled modes at 393.84 (L_3) and 554.7 (L_4) cm^{-1} [53,54]. The $A_g^{(6)}$ phonon mode appears almost at the same spectral position as the sapphire substrate phonon mode at ~ 417 cm^{-1}. The $A_g^{(3)}$ phonon mode is the intense Raman peak reported for the bulk ($\bar{2}01$) β-Ga_2O_3 substrates [53,55] which we use to show the effect of annealing. The full-width half maximum (FWHM) of the $A_g^{(3)}$ peak of β-Ga_2O_3 is 9.8 cm^{-1} for as-grown sample, and 12.25 cm^{-1} for annealed sample. The FWHM varies between 3 cm^{-1} for highest quality bulk crystal to 50 cm^{-1} for highly defective material [51]. The moderate FWHM values for β-Ga_2O_3 thin films indicate a good quality crystal with non-negligible defect concentrations. The broadening of the Raman peak is the result of phonon lifetime reduction, due to the scattering caused by point defects, interface, and residual stress [51]. The $A_g^{(3)}$ peak position is at 198.7 cm^{-1} for the as-grown sample, and 199.4 cm^{-1} for the annealed sample, indicates the presence of residual stress. Both samples have the same β-Ga_2O_3/sapphire interface. So, the broadening or FWHM difference of $A_g^{(3)}$ can originate from point defects. The Raman peak width Γ can be related to the phonon mean free path l [56],

$$l = \frac{s}{\sqrt{\Gamma \omega_0}} \tag{7}$$

where s is the dispersion parameter, and ω_0 is the band center position. The cubed inverse of the phonon mean free path (l^{-3} cm^{-3}) quantifies point defect concentration [51]. The annealed β-Ga_2O_3 has a higher point defect concentration as qualitatively calculated from the FWHM. The increase in point defect concentration with annealing probably comes from the increase in the gallium vacancy (V_{Ga}) at high temperatures, and diffusion of oxygen through already grown Ga_2O_3 in the form of oxygen interstitials (O_i) due to the favorable formation energies for V_{Ga} and O_i in β-Ga_2O_3 in an oxygen-excess environment as shown in Fig. 3d.

5. Conclusion

In summary, we presented a comprehensive calculation and analysis of defect properties in the corundum, monoclinic, and orthorhombic Ga_2O_3 phases. We extended the defect analysis beyond a specific type of point defect in a phase to every possible type of point defect in all of the Ga_2O_3 phases with bandgaps using a unique set of DFT parameterization, which was backed by the experiments. The dominant type of point defect is facilitated by the low defect formation energy in a growth environment (Ga- or O-rich). The Ga-rich growth environment in all Ga_2O_3 phases favors the spontaneous formation of oxygen vacancies with concentrations that can reach as high as 10^{21} cm^{-3}. For example, the O-rich environment significantly reduces oxygen vacancies, as high as ~ 10^{11} cm^{-3} in α-Ga_2O_3. In an O-rich environment, the net intrinsic defects density mostly depends on the metal vacancy, interstitial, and antisite defects with a concentration of 10^{13}-10^{17} cm^{-3} in various Ga_2O_3 phases. The charge transition levels in all phases stay at the deep levels within the bandgap and hence can be referred to as deep-level defects. In theory, the intrinsic defect concentration keeps increasing with temperature (shown up to 1130 °C), and the Ga-/O-rich condition is considered extreme. In experiments, the presence of Ga and O are optimized to obtain high-quality Ga_2O_3 thin films, and the growth of Ga_2O_3 phases occurs in the 550–850 °C temperature range. A qualitative correlation was made between formation energies obtained from theoretical calculations and point defect concentration derived from Raman spectroscopy. Such calculations can be used to describe the variation in Ga_2O_3 material properties and engineer Ga_2O_3-based devices.

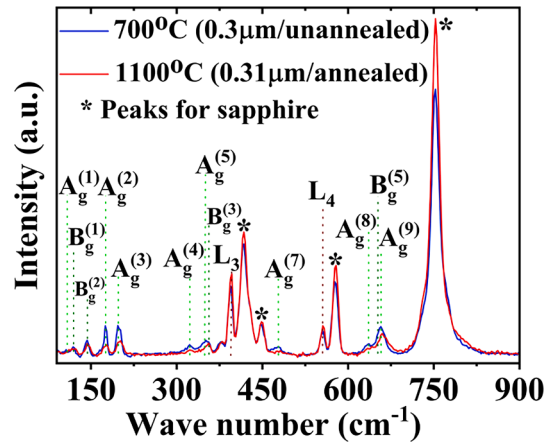

Fig. 6. Raman spectra of β-Ga_2O_3 ($\bar{2}01$) surface for samples grown at 700 °C and annealed at 1100 °C in an oxygen environment.

CRediT authorship contribution statement

Mohi Uddin Jewel: Conceptualization, Data curation, Formal analysis, Funding acquisition, Investigation, Methodology, Writing - original draft, Writing - review & editing. **Samiul Hasan:** Writing - review & editing. **Iftikhar Ahmad:** Supervision.

Declaration of Competing Interest

The authors declare the following financial interests/personal relationships which may be considered as potential competing interests: [IFTIKHAR AHMAD reports financial support was provided by National Science Foundation (NSF award No. 2124624)].

Data availability

Data will be made available on request.

Acknowledgment

This work was supported by the National Science Foundation (NSF) award No. 2124624, managed by Dr. Dominique Degeneis. We acknowledge the computational resources provided by Research Computing (RC) in the Division of Information Technology at the University of South Carolina. We thank Md Nur K Alam, Ph.D. from IMEC, Belgium for helping with the calculations. We are also grateful for the contributions of the summer undergraduate interns Kiyona Trevino and Tyrese Smalley.

Data Availability

The data that support the findings of this study are available from the corresponding author upon reasonable request.

Appendix A. Supplementary material

Supplementary data to this article can be found online at https://doi.org/10.1016/j.commatsci.2022.111950.

References

[1] S.J. Pearton, J. Yang, P.H. Cary IV, F. Ren, J. Kim, M.J. Tadjer, M.A. Mastro, A review of Ga2O3 materials, processing, and devices, Appl. Phys. Rev. 5 (2018) 11301.

[2] S. Liu, Y. Yuan, L. Huang, J. Zhang, T. Wang, T. Li, J. Kang, W. Luo, Z. Chen, X. Sun, X. Wang, Drive High Power UVC-LED Wafer into Low-Cost 4-Inch Era: Effect of Strain Modulation, Adv. Funct. Mater. 32 (2022) 2112111, https://doi.org/10.1002/adfm.202112111.

[3] S. Hasan, M.U. Jewel, S.G. Karakalos, M. Gaevski, I. Ahmad, Comparative spectroscopic study of aluminum nitride grown by MOCVD in H2 and N2 reaction environment, Coatings. 12 (2022) 924.

[4] X. She, A.Q. Huang, O. Lucia, B. Ozpineci, Review of silicon carbide power devices and their applications, IEEE Trans. Ind. Electron. 64 (2017) 8193–8205.

[5] M.U. Jewel, M.D. Alam, S. Mollah, K. Hussain, V. Wheeler, C. Eddy, M. Gaevski, G. Simin, M.V.S. Chandrashekhar, A. Khan, Trap characterization in ultra-wide bandgap Al0. 65Ga0. 4N/Al0. 4Ga0. 6N MOSHFET's with ZrO2 gate dielectric using optical response and cathodoluminescence, Appl. Phys. Lett. 115 (2019) 213502.

[6] Z. Guo, A. Verma, X. Wu, F. Sun, A. Hickman, T. Masui, A. Kuramata, M. Higashiwaki, D. Jena, T. Luo, Anisotropic thermal conductivity in single crystal β-gallium oxide, Appl. Phys. Lett. 106 (2015), 111909, https://doi.org/10.1063/1.4916078.

[7] A.J. Green, J. Speck, G. Xing, P. Moens, F. Allerstam, K. Gumaelius, T. Neyer, A. Arias-Purdue, V. Mehrotra, A. Kuramata, K. Sasaki, S. Watanabe, K. Koshi, J. Blevins, O. Bierwagen, S. Krishnamoorthy, K. Leedy, A.R. Arehart, A.T. Neal, S. Mou, S.A. Ringel, A. Kumar, A. Sharma, K. Ghosh, U. Singisetti, W. Li, K. Chabak, K. Liddy, A. Islam, S. Rajan, S. Graham, S. Choi, Z. Cheng, M. Higashiwaki, β-Gallium oxide power electronics, APL Mater. 10 (2022) 29201, https://doi.org/10.1063/5.0060327.

[8] J.H. Leach, K. Udwary, J. Rumsey, G. Dodson, H. Splawn, K.R. Evans, Halide vapor phase epitaxial growth of β-Ga2O3 and α-Ga2O3 films, APL Mater. 7 (2019) 22504.

[9] D. Shinohara, S. Fujita, Heteroepitaxy of corundum-structured α-Ga2O3 thin films on α-Al2O3 substrates by ultrasonic mist chemical vapor deposition, Jpn. J. Appl. Phys. 47 (2008) 7311.

[10] G. Pozina, C.-W. Hsu, N. Abrikossova, M.A. Kaliteevski, C. Hemmingsson, Development of β-Ga2O3 layers growth on sapphire substrates employing modeling of precursors ratio in halide vapor phase epitaxy reactor, Sci. Rep. 10 (2020) 1–9.

[11] F. Boschi, M. Bosi, T. Berzina, E. Buffagni, C. Ferrari, R. Fornari, Hetero-epitaxy of ε-Ga2O3 layers by MOCVD and ALD, J. Cryst. Growth. 443 (2016) 25–30.

[12] G.T. Dang, T. Kawaharamura, M. Furuta, M.W. Allen, Mist-CVD Grown Sn-Doped $ \alpha $ -Ga2O3 MESFETs, IEEE Trans. Electron Devices. 62 (2015) 3640–3644, https://doi.org/10.1109/TED.2015.2477438.

[13] Y. Lv, J. Ma, W. Mi, C. Luan, Z. Zhu, H. Xiao, Characterization of β-Ga2O3 thin films on sapphire (0001) using metal-organic chemical vapor deposition technique, Vacuum. 86 (2012) 1850–1854, https://doi.org/10.1016/j.vacuum.2012.04.019.

[14] S. Ghose, S. Rahman, L. Hong, J.S. Rojas-Ramirez, H. Jin, K. Park, R. Klie, R. Droopad, Growth and characterization of β-Ga2O3 thin films by molecular beam epitaxy for deep-UV photodetectors, J. Appl. Phys. 122 (2017) 95302, https://doi.org/10.1063/1.4985855.

[15] N. Allen, M. Xiao, X. Yan, K. Sasaki, M.J. Tadjer, J. Ma, R. Zhang, H. Wang, Y. Zhang, Vertical Ga 2 O 3 Schottky barrier diodes with small-angle beveled field plates: A Baliga's figure-of-merit of 0.6 GW/cm 2, IEEE Electron Device Lett. 40 (2019) 1399–1402.

[16] M. Budde, D. Splith, P. Mazzolini, A. Tahraoui, J. Feldl, M. Ramsteiner, H. von Wenckstern, M. Grundmann, O. Bierwagen, SnO/β-Ga2O3 vertical pn heterojunction diodes, Appl. Phys. Lett. 117 (2020), 252106, https://doi.org/10.1063/5.0031442.

[17] M. Higashiwaki, K. Sasaki, A. Kuramata, T. Masui, S. Yamakoshi, Gallium oxide (Ga2O3) metal-semiconductor field-effect transistors on single-crystal β-Ga2O3 (010) substrates, Appl. Phys. Lett. 100 (2012) 13504, https://doi.org/10.1063/1.3674287.

[18] Y. Oshima, E.G. Víllora, Y. Matsushita, S. Yamamoto, K. Shimamura, Epitaxial growth of phase-pure ε-Ga2O3 by halide vapor phase epitaxy, J. Appl. Phys. 118 (2015) 85301, https://doi.org/10.1063/1.4929417.

[19] S. Yusa, D. Oka, T. Fukumura, High-κ dielectric ε-Ga2O3 stabilized in a transparent heteroepitaxial structure grown by mist CVD at atmospheric pressure, CrystEngComm. 22 (2020) 381–385, https://doi.org/10.1039/C9CE01532A.

[20] H.Y. Playford, A.C. Hannon, E.R. Barney, R.I. Walton, Structures of uncharacterised polymorphs of gallium oxide from total neutron diffraction, Chem. Eur. J. 19 (2013) 2803–2813.

[21] M. Biswas, H. Nishinaka, Thermodynamically metastable α-, ε- (or κ-), and γ-Ga2O3: From material growth to device applications, APL Mater. 10 (2022) 60701, https://doi.org/10.1063/5.0085360.

[22] A.M. Hassanien, A.A. Atta, M.M. El-Nahass, S.I. Ahmed, A.A. Shaltout, A.M. Al-Baradi, A. Alodhayb, A.M. Kamal, Effect of annealing temperature on structural and optical properties of gallium oxide thin films deposited by RF-sputtering, Opt. Quantum Electron. 52 (2020) 194, https://doi.org/10.1007/s11082-020-02306-8.

[23] D. Yang, B. Kim, J. Oh, T.H. Lee, J. Ryu, S. Park, S. Kim, E. Yoon, Y. Park, H. W. Jang, α-Gallium Oxide Films on Microcavity-Embedded Sapphire Substrates Grown by Mist Chemical Vapor Deposition for High-Breakdown Voltage Schottky Diodes, ACS Appl. Mater. Interfaces. 14 (2022) 5598–5607, https://doi.org/10.1021/acsami.1c21845.

[24] J.L. Lyons, C.G. Van de Walle, Computationally predicted energies and properties of defects in GaN, Npj Comput. Mater. 3 (2017) 12, https://doi.org/10.1038/s41524-017-0014-2.

[25] M.N.K. Alam, S. Clima, B.J. O'Sullivan, B. Kaczer, G. Pourtois, M. Heyns, J. Van Houdt, First principles investigation of charge transition levels in monoclinic, orthorhombic, tetragonal, and cubic crystallographic phases of HfO2, J. Appl. Phys. 129 (2021) 84102, https://doi.org/10.1063/5.0033957.

[26] H. Peelaers, C.G. Van de Walle, Brillouin zone and band structure of β-Ga2O3, Phys. Status Solidi. 252 (2015) 828–832, https://doi.org/https://doi.org/10.1002/pssb.201451551.

[27] S. Poncé, F. Giustino, Structural, electronic, elastic, power, and transport properties of β− Ga 2 O 3 from first principles, Phys. Rev. Res. 2 (2020) 33102.

[28] K. Ghosh, U. Singisetti, Ab initio velocity-field curves in monoclinic β-Ga2O3, J. Appl. Phys. 122 (2017) 35702.

[29] A. Kyrtsos, M. Matsubara, E. Bellotti, On the feasibility of p-type Ga2O3, Appl. Phys. Lett. 112 (2018) 32108.

[30] D. Wickramaratne, J.B. Varley, J.L. Lyons, Donor doping of corundum (AlxGa1−x) 2O3, Appl. Phys. Lett. 121 (2022) 42110, https://doi.org/10.1063/5.0096394.

[31] S.B. Cho, R. Mishra, Epitaxial engineering of polar ε-Ga2O3 for tunable two-dimensional electron gas at the heterointerface, Appl. Phys. Lett. 112 (2018), 162101.

[32] S. Śmiga, L.A. Constantin, Unveiling the Physics Behind Hybrid Functionals, J. Phys. Chem. A. 124 (2020) 5606–5614, https://doi.org/10.1021/acs.jpca.0c04156.

[33] Y.Z. Abdullahi, S. Ahmad, A.A. Ibrahim, Effects of the Hubbard U correction on the electronic and magnetic properties of the tetragonal V2P2 sheet, RSC Adv. 11 (2021) 35061–35068, https://doi.org/10.1039/D1RA07558F.

[34] T. Zacherle, P.C. Schmidt, M. Martin, Ab initio calculations on the defect structure of β-Ga 2 O 3, Phys. Rev. B. 87 (2013), 235206.

[35] T. Kobayashi, T. Gake, Y. Kumagai, F. Oba, Y. Matsushita, Energetics and electronic structure of native point defects in α-Ga2O3, Appl. Phys. Express. 12 (2019) 91001.

[36] P. Giannozzi, S. Baroni, N. Bonini, M. Calandra, R. Car, C. Cavazzoni, D. Ceresoli, G.L. Chiarotti, M. Cococcioni, I. Dabo, QUANTUM ESPRESSO: a modular and open-source software project for quantum simulations of materials, J. Phys. Condens. Matter. 21 (2009), 395502.

[37] P. Giannozzi, O. Andreussi, T. Brumme, O. Bunau, M.B. Nardelli, M. Calandra, R. Car, C. Cavazzoni, D. Ceresoli, M. Cococcioni, Advanced capabilities for materials modelling with Quantum ESPRESSO, J. Phys. Condens. Matter. 29 (2017), 465901.

[38] G. Prandini, A. Marrazzo, I. Castelli, N. Mounet, E. Passaro, N. Marzari, A standard solid state pseudopotentials, SSSP) library optimized for precision and efficiency, Mater. Cloud Arch., 2021.

[39] J. Buckeridge, Equilibrium point defect and charge carrier concentrations in a material determined through calculation of the self-consistent Fermi energy, Comput. Phys. Commun. 244 (2019) 329–342.

[40] C.G. Van de Walle, J. Neugebauer, First-principles calculations for defects and impurities: Applications to III-nitrides, J. Appl. Phys. 95 (2004) 3851–3879, https://doi.org/10.1063/1.1682673.

[41] C. Freysoldt, J. Neugebauer, C.G. Van de Walle, Fully Ab Initio Finite-Size Corrections for Charged-Defect Supercell Calculations, Phys. Rev. Lett. 102 (2009) 16402, https://doi.org/10.1103/PhysRevLett.102.016402.

[42] C. Freysoldt, J. Neugebauer, C.G. Van de Walle, Electrostatic interactions between charged defects in supercells, Phys. Status Solidi. 248 (2011) 1067–1076, https://doi.org/10.1002/pssb.201046289.

[43] A. Sharma, U. Singisetti, Low field electron transport in α − G a 2 O 3: An ab initio approach, Appl. Phys. Lett. 118 (2021) 32101, https://doi.org/10.1063/5.0027787.

[44] M. Passlack, N.E.J. Hunt, E.F. Schubert, G.J. Zydzik, M. Hong, J.P. Mannaerts, R. L. Opila, R.J. Fischer, Dielectric properties of electron-beam deposited Ga2O3 films, Appl. Phys. Lett. 64 (1994) 2715–2717, https://doi.org/10.1063/1.111452.

[45] I. Chatratin, F.P. Sabino, P. Reunchan, S. Limpijumnong, J.B. Varley, C.G. Van de Walle, A. Janotti, Role of point defects in the electrical and optical properties of ${\mathrm{In}}_{2}{\mathrm{O}}_{3}$, Phys. Rev. Mater. 3 (2019) 74604, https://doi.org/10.1103/PhysRevMaterials.3.074604.

[46] J. Wei, L. Jiang, M. Huang, Y. Wu, S. Chen, Intrinsic Defect Limit to the Growth of Orthorhombic HfO2 and (Hf, Zr)O2 with Strong Ferroelectricity: First-Principles Insights, Adv. Funct. Mater. 31 (2021) 2104913, https://doi.org/https://doi.org/10.1002/adfm.202104913.

[47] C.-Y. Huang, R.-H. Horng, D.-S. Wuu, L.-W. Tu, H.-S. Kao, Thermal annealing effect on material characterizations of β-Ga2O3 epilayer grown by metal organic chemical vapor deposition, Appl. Phys. Lett. 102 (2013) 11119.

[48] N. Makeswaran, A.K. Battu, E. Deemer, C.V. Ramana, Crystal Growth and Structure-Property Optimization of Thermally Annealed Nanocrystalline Ga2O3 Films, Cryst. Growth Des. 20 (2020) 2893–2903.

[49] R.S. Berg, P.Y. Yu, E.R. Weber, Raman spectroscopy of intrinsic defects in electron and neutron irradiated GaAs, Appl. Phys. Lett. 47 (1985) 515–517.

[50] I. Lorite, P. Díaz-Carrasco, M. Gabás, J.F. Fernández, J.L. Costa-Krämer, Correlation between intrinsic defect and carrier transport in ZnO thin films by confocal Raman spectroscopy, Mater. Lett. 109 (2013) 167–171.

[51] V. Lughi, D.R. Clarke, Defect and stress characterization of AlN films by Raman spectroscopy, Appl. Phys. Lett. 89 (2006), 241911, https://doi.org/10.1063/1.2404938.

[52] G. Seryogin, F. Alema, N. Valente, H. Fu, E. Steinbrunner, A.T. Neal, S. Mou, A. Fine, A. Osinsky, MOCVD growth of high purity Ga2O3 epitaxial films using trimethylgallium precursor, Appl. Phys. Lett. 117 (2020), 262101.

[53] C. Kranert, C. Sturm, R. Schmidt-Grund, M. Grundmann, Raman tensor elements of β-Ga2O3, Sci. Rep. 6 (2016) 1–9.
[54] A. Fiedler, M. Ramsteiner, Z. Galazka, K. Irmscher, Raman scattering in heavily donor doped β-Ga2O3, Appl. Phys. Lett. 117 (2020), 152107.
[55] Y. Song, P. Ranga, Y. Zhang, Z. Feng, H.-L. Huang, M.D. Santia, S.C. Badescu, C. U. Gonzalez-Valle, C. Perez, K. Ferri, R.M. Lavelle, D.W. Snyder, B.A. Klein, J. Deitz, A.G. Baca, J.-P. Maria, B. Ramos-Alvarado, J. Hwang, H. Zhao, X. Wang, S. Krishnamoorthy, B.M. Foley, S. Choi, Thermal Conductivity of β-Phase Ga2O3 and (AlxGa1–x)2O3 Heteroepitaxial Thin Films, ACS Appl. Mater. Interfaces. 13 (2021) 38477–38490, https://doi.org/10.1021/acsami.1c08506.
[56] L.A. Falkovsky, J.M. Bluet, J. Camassel, Strain relaxation at the $3C\ensuremath{-}\mathrm{S}\mathrm{i}\mathrm{C}/\mathrm{S}\mathrm{i}$ interface: Raman scattering experiments, Phys. Rev. B. 57 (1998) 11283–11294, https://doi.org/10.1103/PhysRevB.57.11283.